Journal of Energy Storage 90 (2024) 111917

Contents lists available at ScienceDirect

Journal of Energy Storage

journal homepage: www.elsevier.com/locate/est

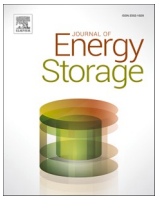

Research Papers

Thermochemical battery prototypes with conductive heat extraction

Lucie Desage, Terry D. Humphries *, Mark Paskevicius, Craig E. Buckley

Physics and Astronomy, School of Electrical Engineering, Computing and Mathematical Sciences, Institute for Energy Transition, Curtin University, U1987, Perth, WA 6845, Australia

ARTICLE INFO

Keywords:
Energy storage
Thermochemical battery
Calcium carbonate
Conduction
Prototype

ABSTRACT

Thermochemical energy storage is a viable option for large-scale storage of renewable energy. Functional storage systems require a high cycling capacity and an efficient heat extraction unit to guarantee reliable energy storage and subsequent power production. This article investigates the performance of thermochemical battery prototypes that use conductive heat extraction via metallic rods. The thermodynamics and kinetics of the storage material, $CaCO_3$-Al_2O_3 (20 wt%), used in the prototypes, were studied along with the cyclic carbon dioxide sorption capacity, which was retained at 60 %. The reaction thermodynamics and kinetics of this doped $CaCO_3$ compound are similar to those reported for pure calcium carbonate ($\Delta H_{des} = 173 \pm 10$ kJ.mol^{-1} CO_2 and $\Delta S_{des} = 147 \pm 9$ J.mol^{-1} CO_2·K^{-1}). The two prototypes were constructed using either a stainless-steel rod or a stainless-steel tube with a copper core as conductive heat exchanger. The thermochemical battery prototypes (~1 kg) cycled >30 times, with thermal charging (calcination) and discharging (carbonation) at ~900 °C. The storage material is sensitive to the operating conditions of pressure and temperature, which influence the formation of various calcium aluminium oxide compounds that either catalyse or inhibit the cyclic capacity. The carbon dioxide sorption capacity in the prototypes was found to be limited (20 %) and capacity loss was correlated to the temperature distribution through the storage material and limited by the heat transfer rate of the heat extraction system. The heat transfer performance of the stainless-steel rod was inadequate, while the copper core allowed for better system performance.

1. Introduction

The drastic increase in global greenhouse gas (GHG) emissions is triggering climatic events that threaten biodiversity and human societies [1]. The mitigation of the effects of climate change requires abstaining from fossil fuels and promoting the utilisation of renewable energy sources, such as wind and solar [1]. Energy storage systems are crucial to cope with the intermittency of renewables and ensure their ability to cover global energy needs. Electrochemical batteries based on Li-ion enable the utilisation of clean electricity, particularly for mobility applications, such as electric vehicles [2]. However, the production of electrochemical batteries for global-scale energy storage is questioned because of the limited abundance of some critical minerals, and the underlying environmental and societal impacts related to their production [3].

Thermal Energy Storage (TES) is an alternative energy storage option for large-scale power production facilities, with potentially lower environmental impact and the possibility to store energy at low-cost with manageable efficiencies [3,4]. Sensible, latent, and thermochemical heat storage (TCES) are distinctive forms of TES, respectively based on a material's heat capacity, phase changes, or chemical reactions. Fig. 1 depicts the working principle of a TCES cycle. When charging, material A absorbs the thermal energy by decomposing into B and C, which can be stored separately until heat is required by reforming material A.

High cyclic reversibility of the thermochemical reactions, depicted in Fig. 1, allows for the application of TCES materials in a thermochemical battery (TCB). The battery is charged by delivering thermal energy to the storage material, which triggers an endothermic chemical reaction. The exothermic reverse reaction releases the stored thermal energy representing the battery discharging pathway. Excess energy from renewables, such as wind and solar, can be used to charge the TCB, as well as waste heat from energy heavy industries [6]. Once the battery is charged, the capacity does not degrade over time as the energy is stored in the chemical bonds of the stable decomposition products.

Abbreviations: ASW, Alumino Silicate wool; GHG, Greenhouse Gas; HTF, Heat Transfer Fluid; o. d., Outer diameter; SR-XRD, In situ synchrotron radiation powder XRD; SS, Stainless-steel (316); TCB, Thermochemical Battery; TCES, Thermochemical Energy Storage; TES, Thermal Energy Storage; XRD, Powder X-Ray diffraction.

* Corresponding author.
E-mail address: terry_humphries81@hotmail.com (T.D. Humphries).

https://doi.org/10.1016/j.est.2024.111917
Received 4 September 2023; Received in revised form 9 April 2024; Accepted 28 April 2024
Available online 4 May 2024

Nomenclature

β	Heating rate [K.min^{-1}]
ΔH	Reaction enthalpy [kJ.mol^{-1}]
ΔS	Reaction entropy [J.mol^{-1}.K^{-1}]
κ	Thermal conductivity [W.m^{-1}.K^{-1}]
λ	Wavelength [Å]
A	Pre-exponential factor [s^{-1}]
d	Distance between thermocouples [m]
E_a	Activation energy [kJ.mol^{-1}]
M_{CO_2}	Molar mass of carbon dioxide [g.mol^{-1}]
m_t	Total mass [g]
P_{eq}	Equilibrium pressure [bar]
q	Heat flux density with subscript c for charging and d for discharging [W.m^{-2}]
r	Reacted fraction
R	Universal gas constant: 8.3145 J.mol^{-1}.K^{-1}
S	Cross-section area [m^2]
t	Time period [s]
T	Temperature [K]
T_p	Peak temperature [K]
Q	Heat transfer rate [W]
Q_{th}	Power generated by the storage material [W]
W_{th}	Thermal power [W]

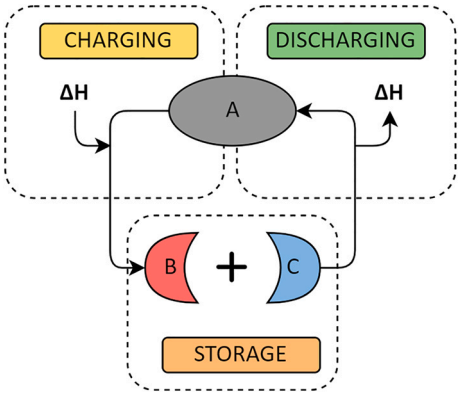

Fig. 1. Schematic of a thermochemical heat storage (TCES) cycle [5].

However, each TCB material has optimal operational temperature and pressure, which are required to maintain adequate reaction kinetics and thermodynamics. Upon discharging, the heat of reaction released by the TCB can operate a heat engine, such as a Stirling engine or a steam turbine, to generate power by converting heat into mechanical energy, then to electricity. The conversion efficiency of heat energy to electricity is governed by thermodynamic restraints explained by the Carnot limit, which are maximised at higher operating temperatures. Fig. 2 shows a schematic of the aforementioned TCB system. Prototypes using metal hydrides as a TCES material and a heat transfer fluid (HTF) to extract the heat from the system have been constructed, operating at temperatures below 500 °C [7–9]. However, to ensure 25 % efficiency of a 40 kW Stirling engine, the lower operating temperature of the hot side of the engine is required to be ~700 °C [10]. Thus, higher temperature TCES

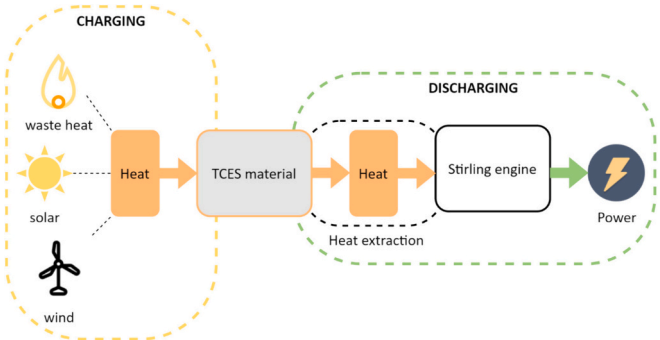

Fig. 2. Schematic of a thermochemical battery (TCB) for the storage of renewables combined with a Stirling engine for electrical power production.

systems are required to provide adequate thermal-electric conversion efficiencies and reduce the footprint and cost of energy production.

TCES materials can include various types of compounds, such as hydrides, hydroxides, and oxides, which are compared in numerous review articles [11–13]. These different systems vary in energy storage density, operating temperatures and cost [14]. A recent study highlighted the potential utilisation of metal carbonates for high-temperature TCES and discussed their integration into a TCB, emphasising the crucial role of the heat extraction system to enable efficient power production [5]. A cost-effective storage material option for TCBs operating at a suitable temperature is calcium carbonate. $CaCO_3$ undergoes a reversible calcination above 880 °C at 1 bar CO_2 (eq. 1) with a reaction enthalpy of 165.7 kJ.mol^{-1}, which corresponds to a volumetric energy density of 4492 MJ.m^{-3}, offering the potential to generate 1.247 MWh_{th}.m^{-3} [5,15]. Thus, calcium carbonate is an ideal candidate for TCES applications at high temperatures because of its high energy density potential and abundancy [13,16].

$$CaCO_{3(s)} \rightleftharpoons CaO_{(s)} + CO_{2(g)} \quad (1)$$

Extensive studies on the thermodynamics and kinetic mechanisms of the reversible thermochemical reactions (calcination/carbonation) have been undertaken on the $CaCO_3$ system [17,18]. Experimental results agree on the drastic loss in CO_2 storage capacity over several cycles due to powder sintering and pore plugging [13,19–22]. For TCB applications, the storage capacity of the material must remain stable over thousands of cycles to maintain a viable TCB operational lifetime. A reduction in the cyclic capacity of 75 % for the $CaCO_3$/CaO system is not acceptable to build reliable TCBs [19,22,23]. Doping with additives, such as SiO_2, TiO_2, ZrO_2 and Al_2O_3, enhances the cycling capacity of the $CaCO_3$/CaO system [15,24,25]. The presence of additives affects the porosity, particle-segregation of the materials, and hinders sintering, which results in faster reaction kinetics and higher gas sorption capacity over reaction cycles. The ratio of calcium carbonate and additive must be such that the theoretical maximum sorption capacity and the cost of the system remain competitive with alternative energy storage options. Ma et al. [26] conducted a density functional theory (DFT) study and measured the thermodynamic stabilities of various $Ca_xAl_yO_z$ compounds, which confirmed the thermal stability of particular reaction additives and provided information on their interaction with CaO. Sintering is hindered by the bonding of CaO with the additive, which could also restrict the carbonation sites available, hence the utilisation of a low ratio of corundum (Al_2O_3) is advised to preserve the CO_2 capacity [26]. Particularly, Møller et al. determined that when 20 wt% Al_2O_3 is mixed with $CaCO_3$, the formation of the inert support $Ca_5Al_6O_{14}$ (eq. 2) promotes CO_2 diffusion, allowing for 90 % energy storage capacity over 500 cycles at 900 °C [15].

$$5CaO_{(s)} + 3Al_2O_{3(s)} \longrightarrow Ca_5Al_6O_{14(s)} \quad (2)$$

A prototype TCES reactor without heat extraction using 3.2 kg of

$CaCO_3$-Al_2O_3 (16.7 wt%) demonstrated a reasonably stable capacity over multiple cycles between 900 °C with CO_2 pressures <0.7 for calcination and >5 bar for carbonation, but sintering caused by inadequately high temperatures within the reactor resulted in performance loss [27]. This TCES system can be integrated as a TCB, but the selection of a suitable heat extraction system is made difficult by the high operating temperature around 900 °C. This excludes the use of conventional heat transfer fluids, such as traditional molten salts, and thermal oils [28,29]. Molten alkali, heavy and eutectic metal alloys properties are suitable as HTF for temperatures above 900 °C and possess the required heat transfer efficiency for TCB applications. However, corrosion issues, cost, safety, and compatibility with structural materials remain as some of the major challenges to their implementation [30,31]. Supercritical CO_2 is also promising for HTF use in power generation applications; particularly, supercritical CO_2 power blocks in Concentrated Solar Power plants has a thermal efficiency estimated to be 33–55 % [32]. However, the utilisation of supercritical CO_2 as a high-temperature HTF presents challenges in terms of turbomachinery technical design, material selection, and cost [32].

Radiative heat transfer becomes dominant at high temperatures and may be harnessed or optimised for effective heat delivery [33]. While exploring this mechanism for TCB applications may be beneficial, further investigation is needed to potentially scale up radiative heat exchangers [5,33]. Thus, conduction appears as a feasible and economical method to extract heat from a high-temperature TCES reactor. The use of a conduction-based heat transfer system also avoids the use of mobile liquids at high temperature, which could be advantageous from a maintenance standpoint.

This paper presents an experimental study of two TCB prototypes using conduction through metallic rods as a heat extraction system. The TCES material chosen for these experiments is $CaCO_3$-Al_2O_3 (20 wt%), which has been thoroughly characterised through physical studies, including elucidation of reaction thermodynamics and kinetics. The additional knowledge about the thermodynamics and kinetics of $CaCO_3$-Al_2O_3 (20 wt%) emphasised in this work can contribute to the optimisation of large-scale prototypes using this system. A 316 stainless-steel (SS) rod and a SS tube with a copper core were used as heat transfer media to build two distinct prototypes with ~1 kg of storage material each. The experimental design of each of the prototypes is discussed, along with an evaluation and comparison of their performance. The objective of this experimental study is to assess the feasibility of using conduction as a heat extraction system to power a Stirling engine coupled to a TCB with a focus on system limitations and design considerations.

2. Experimental

2.1. Thermochemical energy storage material

The preparation of the $CaCO_3$-Al_2O_3 (20 wt%) storage material followed the procedure described by Møller et al. [27]. A 6 kg mixture of $CaCO_3$ (Chem-Supply, 98 %) and Al_2O_3 (Sigma-Aldrich, Puriss. ≥98 %) in a weight ratio 1:0.2 was ground in a Latino Design 0.75 kW 304 stainless steel 15 kg Rod Mill with 15 rods. Grinding was undertaken for 30 min followed by dry screening to achieve a particle size of <75 μm. The oversized material was then added back to the mill and the grinding process continued until all material had a particle size of <75 μm. To ensure mixing was complete the material was then ball-milled in a Glen Mills Turbula T2C shaker mixer operating at 160 rpm for 1 h in batches of ~250 g in a custom made 650 mL SS canister containing 55 SS balls, o.d. = 12.7 mm and total mass ~465 g. The resulting ball-milled material was a fine white powder.

2.2. Sieverts measurements

The thermodynamic properties of $CaCO_3$ and $CaCO_3$-Al_2O_3 (20 wt%) were determined using the Sieverts manometric method using Pressure Composition Isotherm (PCI) measurements [34]. A custom-made apparatus was used for the measurements equipped with a Rosemount 3051S manometer (±0.035/0–55 bar), K-type thermocouple and Pt thermistors, with a reference volume of 19.9 cm^3 and a SiC high temperature sample cell (38.1 cm^3). The equation of state for CO_2 was used from the NIST Refprop database [35]. The volume of the sample was calculated assuming a $CaCO_3$-Al_2O_3 (20 wt%) density of 1.85 $g.cm^{-3}$ [15]. The activated $CaCO_3$-Al_2O_3 (20 wt%) sample (0.96 g, 0.52 cm^3) was introduced into the SiC cell and the evolution of the composition was measured by starting at 2 bar CO_2 (Coregas >99 %) for three isotherms (867 °C, 883 °C, and 913 °C). The kinetic desorption curves were obtained by decreasing the CO_2 pressure in steps of ~0.5 bar, maintained until thermodynamic equilibrium was reached (~10 min per step). The plateau pressures P_{eq} (bar) for each isotherm at a particular T enable the determination of a van't Hoff plot, from which the decomposition enthalpy ΔH and entropy ΔS are respectively calculated from the linear slope and intercept using eq. 3, where R is the universal gas constant (8.3145 $J.K^{-1}.mol^{-1}$) [36].

$$ln\left(P_{eq}\right) = \frac{-\Delta H}{R}\left(\frac{1}{T}\right) + \frac{\Delta S}{\mathrm{R}} \tag{3}$$

PCI measurements were also performed with as-supplied $CaCO_3$ to determine and compare its thermodynamics properties with the $CaCO_3$-Al_2O_3 mixture. In this case, the gas evolution was measured starting at 4 bar for four isotherms (870 °C, 890 °C, 910 °C, and 930 °C). The reaction enthalpy and entropy were deduced from the corresponding van't Hoff plot.

CO_2 cycling measurements (desorption/absorption) were performed using 0.21 g (0.11 cm^3) of $CaCO_3$-Al_2O_3 (20 wt%) at a constant temperature of 900 °C for 30 cycles (activation cycles), with desorption under vacuum for 20 min and absorption under a CO_2 pressure of ~3 bar for 30 min. These step times were chosen to ensure that the reactions were complete, either fully desorbed or fully absorbed. Then, test cycles were performed with 1 h absorption and 1 h desorption at 880, 890, 895, 900, 905, 910 and 920 °C. Each temperature was tested with CO_2 absorption at 2.5 bar and desorption at 0.5 bar, as well as absorption at 1.5 bar and desorption at 1 bar. During the test cycles, the system was put under vacuum for at least 20 min to fully desorb the material in between each test.

The CO_2 capacity was calculated assuming a theoretical maximum of 24 wt% of CO_2. This theoretical maximum considers the remaining proportion of $CaCO_3$ that will not react with the Al_2O_3 additive to form the calcium aluminium oxide catalyst (eq. 2). Because the CO_2 capacity represents the ratio of the measured wt% of CO_2 and the theoretical maximum of 24 wt% of CO_2, the calculated capacity shows a value >1 when the catalyst is not yet formed.

2.3. Thermogravimetric analysis

Thermogravimetric analyses were performed on 36.07 mg of activated $CaCO_3$-Al_2O_3 (20 wt%) placed in an alumina crucible (6.8 mm diameter/85 μL) using a Netzsch STA 449 F3 Jupiter apparatus to determine the activation energy of the carbon dioxide desorption and absorption. Under an argon flow of 20 $mL.min^{-1}$, the sample was heated to 900 °C to collect the initial CO_2 desorption data, then cooled down to 100 °C. After a 10 min isotherm at 100 °C, the sample was heated under a CO_2 flow of 80 $mL.min^{-1}$ (~0.8 bar CO_2) and argon flow of 20 $mL.min^{-1}$ to collect the absorption data. The measurement was repeated at different heating rates (20, 10 and 5 $K.min^{-1}$). The peak temperatures T_p at each heating rate β enabled the determination of a Kissinger plot, from which the activation energy E_a is deduced from the linear slope of eq. 4 [37]. The temperature of the DSC was calibrated using In, Zn, Al, Ag and Au reference materials, resulting in a temperature accuracy of ±0.2 °C, while the balance has an accuracy of ±20 μg.

$$ln\left(\frac{\beta}{T_p^2}\right) = ln\left(\frac{AR}{E_a}\right) - \frac{E_a}{RT_p} \quad (4)$$

2.4. Powder X-Ray diffraction

Powder X-Ray diffraction (XRD) was performed in flat-plate geometry mode on a Bruker D8 Advance diffractometer equipped with a CuK$\alpha_{1,2}$ source. The measurement data were collected by a Lynxeye PSD detector in steps of 0.02° of a 5–80° 2θ range. Phase identification was performed using the Bruker EVA software whilst quantification and Rietveld refinement by the TOPAS v.5 software [38,39]. Each of the XRD patterns with their corresponding fitting curves resulting from the Rietveld refinement are presented in the ESI (Fig. S1 to S17).

In situ synchrotron radiation powder XRD (SR-XRD) data were collected at the Australian Synchrotron, Melbourne, Australia, for the activated $CaCO_3$-Al_2O_3 (20 wt%) material, which contains the formed catalyst $Ca_xAl_yO_z$. Powder samples were loaded in quartz capillaries (outer diameter 0.7 mm, wall thickness 0.01 mm) and mounted using Swagelok tube fittings to a vacuum manifold and measured under dynamic vacuum. One-dimensional SR-XRD patterns (monochromatic X-rays with λ = 0.825040(5) Å) were continuously collected using a Mythen microstrip detector with an exposure time of 30 s at two different detector positions in order to cover the entire 2θ range (3–80°) [40]. The capillary was heated up from room temperature to 950 °C at a heating rate of 6 °C.min^{-1} and was continuously oscillating during the data collection through a 100° angle to improve the powder averaging and ensure even heating.

2.5. Thermochemical battery prototypes

2.5.1. Prototype design and manufacture

Two TCB prototypes were constructed from SS fittings (Swagelok and Stirlings). Photographs of the prototype are presented in Fig. S18 (ESI). The cylindrical reactor body had a 6.6 cm inner diameter and length of 22 cm. Six K-type thermocouples (T1 - T6) were attached with SS ring clamps along a 75 cm long heat extraction rod of 1.6 and 1.9 cm outer diameter for prototype 1 and 2, respectively (Fig. S18-a, ESI). T1 to T4 were evenly spaced at ~7 cm intervals inside the reactor, while the distance between T5, T6, and the top of the rod was ~12 cm. The $CaCO_3$-Al_2O_3 storage material was packed in the reactor using manual compression with the heat extraction rod centralised through the reactor (Fig. S18-b, ESI). The rod was sealed at the top of the reactor by a SS Swagelok ferrule. All connections on the reactor body were welded to prevent gas leakage at high temperature. The reactor was insulated with aluminium silicate wool (ASW, ~5 cm) and placed in a box furnace ('background furnace', Furnace Technologies, P44SSK-SCR-OT #2691, Taie controller PFY700), while the outer part of the heat extraction rod was placed in a smaller tube furnace mounted on top of the main background furnace ('dynamic furnace', Ceramic Engineering, Omron controller E5-CN-H) (see Fig. 3). The interface between the two furnaces was also insulated with ASW. The bottom of the reactor was connected to gas lines by SS Swagelok parts, and a SS particle filter mesh was placed at the base of the reactor to prevent powder migration. Table 1 lists the specifications of each prototype.

The carbon dioxide sorption capacity of the TCB prototypes were evaluated over at least 30 cycles using the experimental settings

Table 1
Prototype specifications.

	Prototype 1	Prototype 2
$CaCO_3$-Al_2O_3 (20 wt%) [kg]	1.44	1.28
Reactor body diameter [cm]	6.6	
Reactor body length [cm]	22	
Heat extraction rod		
Length [cm]	75	
Rod material	SS 316	SS 316 tube copper core
Outer diameter [cm]	1.6 (5/8″)	1.9 (3/4″)
Core diameter [cm]	–	1.6 (5/8″)
Core thermal conductivity [W.m^{-1}.K^{-1}]	~26 [41][a]	391.1 [42]

[a] thermal conductivity values between 850 and 950 °C.

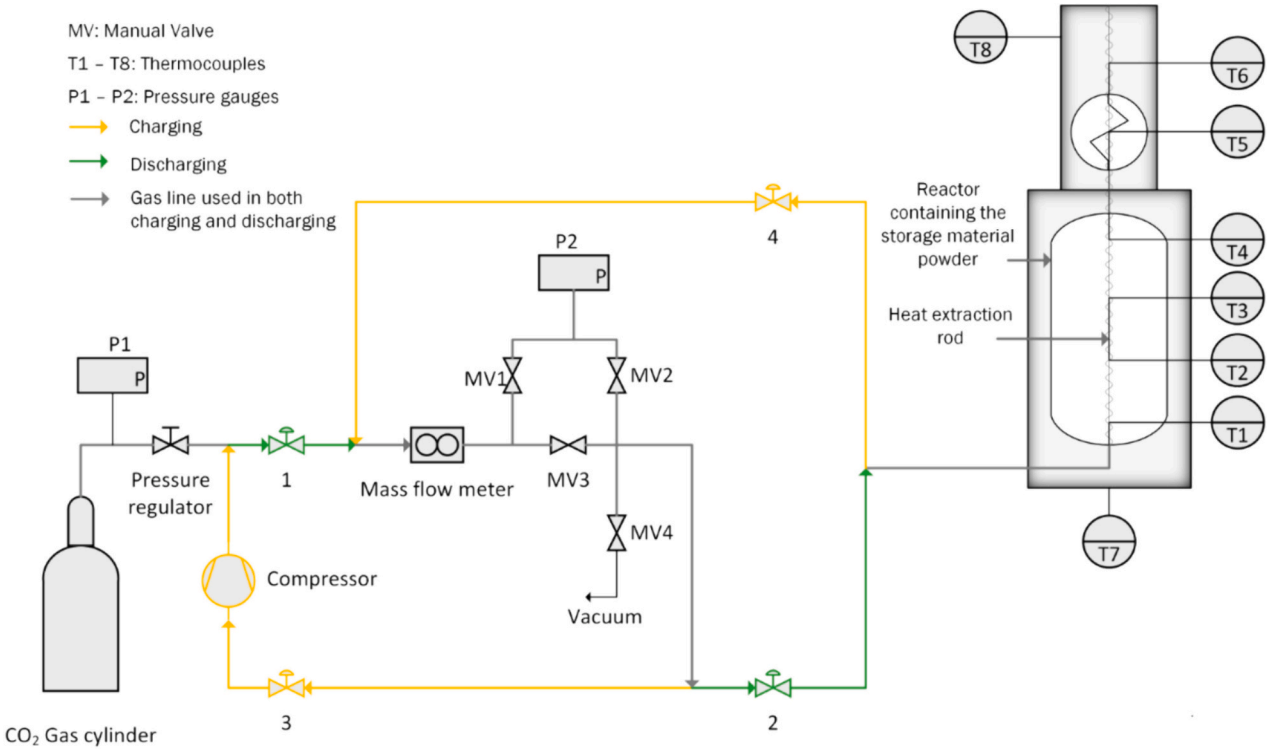

Fig. 3. Process diagram of the TCB prototype's control rig.

presented in Table 2. The operating conditions of pressure and temperature were chosen according to the reversible reaction equilibrium diagram (see Fig. S19, ESI). At a constant temperature of 900 °C, a carbon dioxide pressure of ≤0.5 bar ensures decomposition of the material (battery charging), while a carbon dioxide pressure of 2 bar allows for the carbonation to occur (battery discharging). Thus, each charging and discharging step was triggered by varying the pressure of the system and the heat extraction rod served a dual purpose: (1) injecting heat generated by the higher temperature 'dynamic furnace' into the prototype reactor during charging and (2) extracting heat generated by the storage material during discharging by lowering the 'dynamic furnace' temperature. The step time of 6 h was chosen to run the experiment in conditions that will match real life applications. For example, a TCES system integrated into a power production plant using renewables must store the energy when the renewable source is available, and back up the energy supply when the resource is not available, which can represent many hours.

The TCB reactor was integrated into a gas manifold (Fig. 3) controlled by inhouse software developed using LabVIEW v.2018 (National Instruments). The LabVIEW program collected pressure, temperature, and gas flow data and operated pneumatic gas valves to initiate either CO_2 desorption (charge) or absorption (discharge). A CO_2 gas storage cylinder (volume = 30 L) was used to hold and deliver reaction gas, whilst its pressure (P1) was measured by a Rosemount 3051S pressure transmitter. An Alicat Scientific MC-20SLPM-D mass flow meter was used to collect manifold/reactor pressure, ambient temperature, gas mass flow and volumetric flow data, while a second Rosemount 3051S pressure transmitter also collected manifold/reactor pressure (P2). The software was automated to cycle between charging and discharging based on the temperature of the 'dynamic furnace' (T8), which was programmed to control the TCES system using desired reaction times (see Fig. 3):

i. Charging (CO_2 release): T8≥800 °C: valves 3 and 4 were open, valves 1 and 2 were closed. The carbon dioxide desorbed from the storage material was compressed in the CO_2 gas cylinder by an air driven gas booster (DLE 30-GG MAXIMATOR #475561) with a pressure ratio of 1:20.
ii. Discharging (CO_2 absorption): T8≤500 °C: valves 1 and 2 were open, valves 3 and 4 were closed. The pressure regulator from the storage bottle was set to 2 bar, allowing carbon dioxide to flow into the reactor and be absorbed by the storage material.

The entire gas system was purged several times by vacuum and flushed with carbon dioxide before starting the cycling experiment for both prototypes. The 30 L gas cylinder was initially filled with 4 bar CO_2 (Coregas, <90 wt% CO_2, >10 wt% H_2) to ensure a constant pressure of 2 bar was maintained throughout carbonation by the regulator.

The CO_2 capacity was determined using the volumetric CO_2 flow data collected by the mass flow meter during the cycling experiment of the prototypes. The CO_2 wt% was deduced for each data point (based on CO_2 mass flow to and from the reactor) and the corresponding capacity determined by the ratio of the calculated CO_2 wt% and the theoretical maximum (24 wt% of CO_2). The details of the calculation can be found in the ESI.

Table 2
Experimental settings for prototype cycling.

	Charging	Discharging
Step time [h]	6	
Pressure [bar]	~0.5	2
'Dynamic furnace' temperature (T8) [°C]	950	450
'Background furnace' temperature (T7) [°C]	900–950	
Number of cycles	>30	

2.5.2. Heat extraction through conduction

The expected power, Q_{th} [W], generated by the storage material during the discharge of the TCB for a defined period, t [s], is a function of the carbonation enthalpy, ΔH [kJ.mol^{-1}], and the reacted fraction of carbon dioxide, r, multiplied by the total mass of material, m_t [g], divided by the molar mass of CO_2, M_{CO_2} [g. mol^{-1}]:

$$Q_{th} = \Delta H.10^3 \frac{m_t \times r}{M_{CO_2}} \frac{1}{t} \quad (5)$$

Fourier's law for thermal conduction states that heat transfer through conduction occurs if a thermal gradient exists in the solid, with the heat flowing down the thermal gradient [43]. According to Fourier's law, the heat flux [W.m^{-2}] at the extremity of the rod during charging (q_c) and discharging (q_d) can be calculated using eq. 6 and 7 respectively, where κ [W.m^{-1}.K^{-1}] is the thermal conduction of the rod and d [m] the distance between the thermocouples T1 and T6.

$$q_c = -\kappa \frac{T6 - T1}{d} \quad (6)$$

$$q_d = -\kappa \frac{T1 - T6}{d} \quad (7)$$

The total heat transfer rate, Q [W], by conduction through the rod is then determined by multiplying the corresponding heat flux, q, by the cross-section area of the rod, S [m^2] (eq. 8).

$$Q = q.S \quad (8)$$

SS has a relatively low thermal conductivity (~26 W.m^{-1}.K^{-1} between 850 and 950 °C [41]), while copper is one of the metals with the highest thermal conductivities that have melting points above 900 °C [41,42]. SS is chosen as a heat extraction rod for TCB prototype 1 because of its reasonable corrosion resistance at high temperatures under a carbon dioxide atmosphere despite its relatively low heat transfer performance [27]. The TCB prototype 2 required a SS tube to protect the highly thermally conductive copper core from oxidising in air and carbon dioxide atmosphere at the high temperatures imposed by the experimental conditions [44,45].

The thermal conductivity of the rod used for prototype 2 is estimated considering the contribution of the copper core and the SS tube. The copper core represents 83 % of the cross-section diameter of the rod, therefore the thermal conductivity is estimated as follow:

$$\kappa_2 = 0.83 \times \kappa_{core} + 0.17 \times \kappa_{tube} \quad (9)$$

3. Results and discussions

3.1. TCES material activation and characterisation

3.1.1. CO2 Sorption capacity

It has been noted in previous studies that the $CaCO_3$-Al_2O_3 (20 wt%) system undergoes an activation process where a $Ca_5Al_6O_{14}$ catalyst is formed [15]. Therefore, the material in a full scale prototype would constitute $CaCO_3$-$Ca_5Al_6O_{14}$. As such the physical properties of the catalysed material should be fully understood. Fig. 4 shows the evolution of the CO_2 sorption capacity over the activation and test cycles on a small sample of powder (~ 0.2 g). The CO_2 capacity was calculated considering the theoretical maximum sorption capacity of $CaCO_3$-Al_2O_3 (20 wt%) being 24 wt%, hence a relative capacity of over 1 during the first cycle is possible because $CaCO_3$ had not reacted completely with Al_2O_3 yet [27]. During the activation cycles (Fig. 4-a), the capacity dropped to 0.55 in these rapid sorption steps (20 and 30 min for desorption and absorption, respectively). The test cycles with 1 h absorption at 2.5 bar show a higher capacity, reaching 0.7. This observation indicates that longer absorption times improve the overall carbonation rate, which is expected given the inherent gas-solid reaction kinetics.

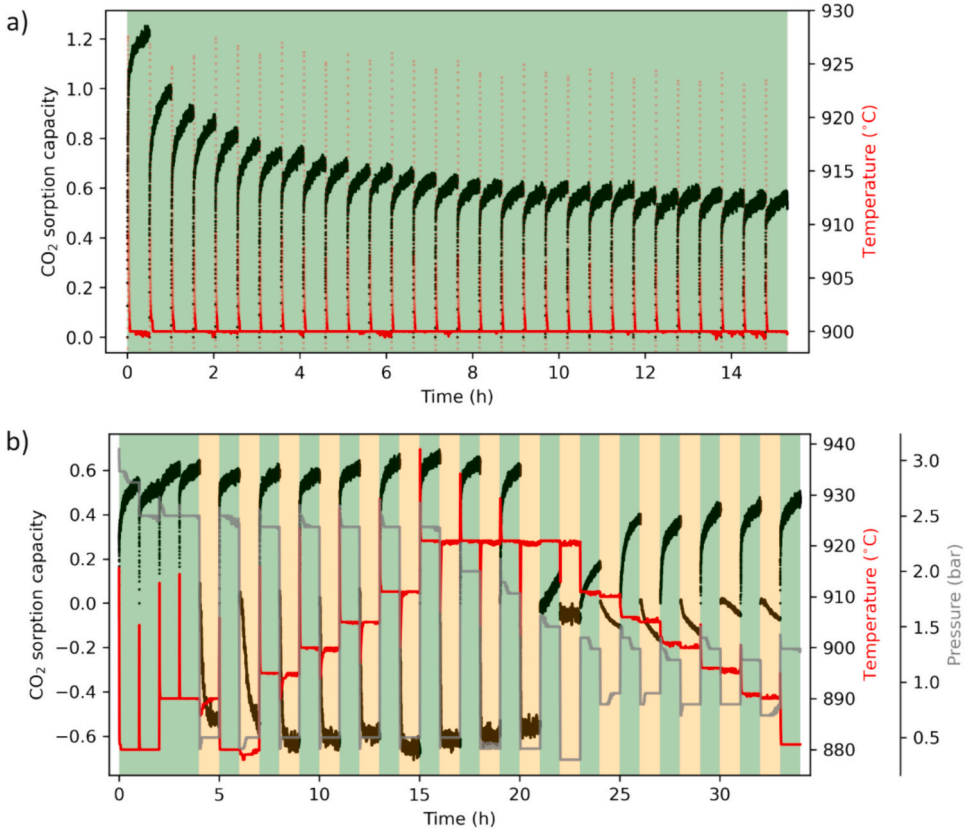

Fig. 4. Cycling conducted in the Sieverts apparatus where the CO_2 sorption capacity of $CaCO_3$-Al_2O_3 (20 wt%) was calculated considering the theoretical maximum achievable CO_2 sorption being 24 wt% of the initial sample mass (i.e. assuming complete conversion to $Ca_xAl_yO_z$) and the temperature of the sample was recorded over time. a) shows the absorption capacity over 30 activation cycles. b) shows the ab/desorption, respectively represented by the green and orange areas, at different sorption temperatures and pressures. (For interpretation of the references to colour in this figure legend, the reader is referred to the web version of this article.)

It is noteworthy that each CO_2 absorption step resulted in considerable thermal spikes within the sample (thermocouple was touching the powder), indicated by the temperature measurement in red in Fig. 4. CO_2 release also resulted in some deviation of the sample temperature but was often not remarkable due to the slower reaction conditions under these pressures. The temperature peaks and troughs observed, respectively during the carbonation and desorption, are proportional to the absorption capacity. The thermodynamics of reaction dictate an equilibrium pressure between $CaCO_3$ and CaO/CO_2, which is temperature dependent (Fig. S19, ESI). When system gas pressures are close to the equilibrium pressure (e.g. 0.5 bar at 880 °C in the first testing regime) then reaction kinetics for CO_2 release are slow, however the same system gas pressure at higher temperature (e.g. 0.5 bar above 900 °C in the first testing regime) are rapid and reach completion. The test cycles at lower absorption pressure (1.5 bar) and desorption at 1 bar (second testing regime) show slower CO_2 absorption and release as these pressures are even closer to the equilibrium pressure. As such, these cycles did not reach completion. The conditions of the activation and test cycles are summarised on the equilibrium diagram in Fig. S19 (ESI).

The XRD pattern (Fig. 5) and quantitative analysis (Table S1, ESI) of ball-milled $CaCO_3$-Al_2O_3 (20 wt%) confirms the presence of 79.2 wt% calcium carbonate, 16.8 wt% alumina and 4.0 wt% of Dolomite is present in the XRD data from the ball-milled material (Fig. 5-i). Dolomite occurs naturally in calcite deposits and could be an impurity in the as-supplied $CaCO_3$ material [46]. After the activation and test cycles (Fig. 4), the XRD pattern (Fig. 5-ii) shows new diffraction peaks corresponding to 18.4 wt% of $CaAl_2O_4$ resulting from the reaction of CaO and Al_2O_3, which acts as an anti-sintering additive. 71 wt% of calcium carbonate and 10.5 wt% of alumina remains (Table S1, ESI). An unknown phase is also observed that was not quantified. This phase was

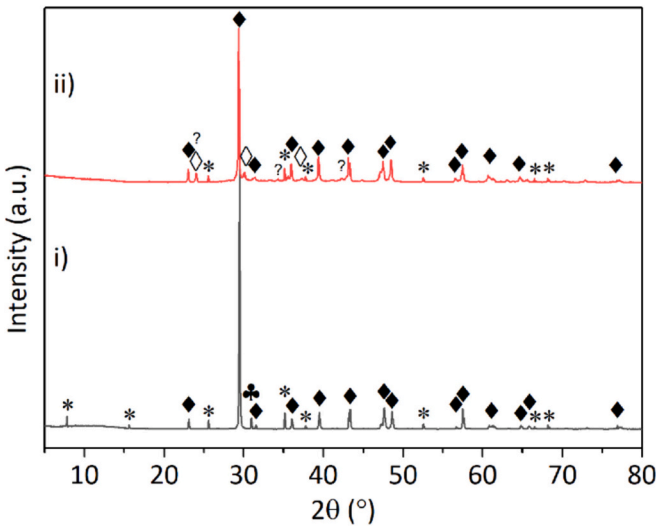

Fig. 5. XRD pattern ($\lambda = 1.5406$ Å) of (i) the ball-milled material, and (ii) after the activation and test cycles in Fig. 4 (Markers: ◆: $CaCO_3$, *: Al_2O_3, ◇: $CaAl_2O_4$, ♣: Dolomite, ? Unknown).

previously determined as unidentifiable [15]. The decrease of the cyclic CO_2 capacity during the activation and test cycles corresponds to the loss of calcium carbonate to form $CaAl_2O_4$. The capacity could potentially decrease further because of the remaining fraction of alumina that could react with additional CaO to form other $Ca_xAl_yO_z$ additives (eq. 2). Also, further reaction of $CaAl_2O_4$ with CaO could form Mayenite (eq. 10)

leading to the reduction of available active sites for the carbonation, which deteriorates the cyclic capacity [26,47].

$$5CaO_{(s)} + 7CaAl_2O_{4(s)} \longrightarrow Ca_{12}Al_{14}O_{33(s)} \quad (10)$$

Another batch of activated $CaCO_3$-Al_2O_3 (20 wt%) powder (activation by 30 ab/desorption cycles respectively under 3 bar for 30 min and vacuum for 20 min at ~900 °C) was analysed by temperature dependant in-situ synchrotron powder X-ray diffraction (SR-XRD) to determine the decomposition process and phase evolution of the material. The activated sample was measured *in vacuo* from room temperature to 950 °C. Fig. 6-a) shows the intensity map of the scans as the temperature increases. Around 450 °C, the Al_2O_3 peak at $2\theta \approx 24°$ disappears, then no major phase changes occur in the material until the temperature reaches

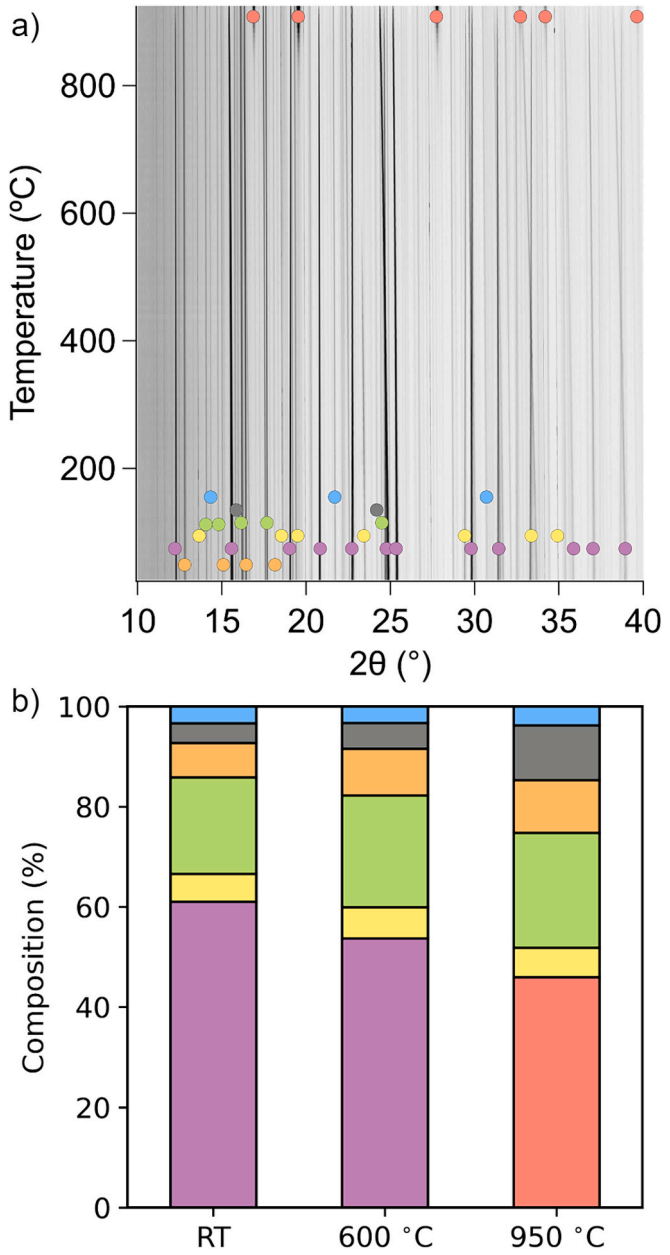

Fig. 6. a) In-situ XRD pattern of activated $CaCO_3$-Al_2O_3 (20 wt%) and b) composition of the activated $CaCO_3$-Al_2O_3 (20 wt%) at different temperatures: room temperature (RT); 600 °C; 950 °C. $CaCO_3$: purple; Al_2O_3: yellow; CaO: red; $Ca_5Al_6O_{14}$: green; $Ca_{12}Al_{14}O_{33}$: orange; $CaAl_2O_4$: grey; $Ca_9Al_6O_{18}$: blue. λ = 0.825040(5) Å. (For interpretation of the references to colour in this figure legend, the reader is referred to the web version of this article.)

~850 °C. At this temperature, the Bragg peaks for $CaCO_3$ gradually diminish, while CaO appears and intensifies over the remaining temperature range. The activated sample initially contained diverse $Ca_xAl_yO_z$ compounds ($Ca_5Al_6O_{14}$, $Ca_{12}Al_{14}O_{33}$, $Ca_9Al_6O_{18}$, $CaAl_2O_4$), which can form depending on the activation conditions (eq. 11) [26].

$$9CaO_{(s)} + 3Al_2O_{3(s)} \longrightarrow Ca_9Al_6O_{18(s)} \quad (11)$$

The amount of $Ca_5Al_6O_{14}$ and Mayenite slightly increases from room temperature to 950 °C (Fig. 6-b). Fig. S20 (scan 124, ESI) illustrates the SR-XRD pattern measured at 950 °C, while Fig. 6-b (950 °C) represents the quantitative Rietveld refinement data. At this temperature, the conversion of $CaCO_3$ into CaO is complete. This data shows that even after activation there can still be $Ca_xAl_yO_z$ formation, reactivity, and compositional changes. This behaviour may allow this additive to provide enhanced anti-sintering behaviour during CO_2 cycling.

3.1.2. Thermodynamics

The PCI curves for both the activated storage material $CaCO_3$-Al_2O_3 (20 wt%) (Fig. 7-a) and as-supplied $CaCO_3$ (Fig. 7-b) were measured to determine their thermodynamics of CO_2 desorption. This data is often used to determine the operational temperature and pressure for TCES materials and to determine their maximum TES capacity. Each PCI curve shows a single plateau characterising the single step decomposition of the materials into the calcium oxide and carbon dioxide. The van't Hoff plots depicted in Fig. 7-c) and d) show the experimentally measured thermodynamics of $\Delta H_{des} = 173 \pm 10$ kJ.mol^{-1} CO_2 and $\Delta S_{des} = 147 \pm 9$ J.mol^{-1} CO_2·K^{-1} for $CaCO_3$-Al_2O_3 (20 wt%) and $\Delta H_{des} = 172 \pm 8$ kJ.mol^{-1} CO_2 and ΔS_{des} 146 ± 7 J.mol^{-1} CO_2·K^{-1} for as-supplied $CaCO_3$, respectively. Considering the measurement uncertainties, the experimental values match each other and the previously reported thermodynamic properties of $CaCO_3$ (enthalpy of 166 kJ.mol^{-1} CO_2 and entropy of 143 J.mol^{-1} CO_2·K^{-1}) [48]. $Ca_xAl_yO_z$ does not take part in the decomposition reaction; thus, the presence of calcium aluminate compounds in the material matrix does not affect the decomposition thermodynamics.

The experimentally measured enthalpy of the $CaCO_3$-Al_2O_3 (20 wt%) system enabled the determination of the reversible reaction equilibrium

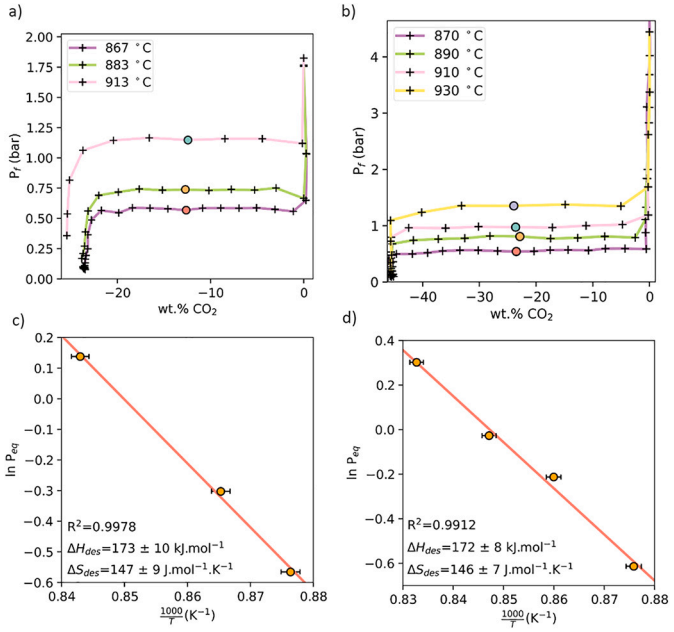

Fig. 7. Pressure Composition Isotherm (PCI) curves during decomposition of a) activated $CaCO_3$-Al_2O_3 (20 wt%) and b) as-supplied $CaCO_3$ showing the plateau pressure points chosen for the determination of their respective van't Hoff plots c) and d).

diagram (Fig. S19, ESI) which was used to determine the optimal operating conditions of pressure and temperature for the cycling of the TCB prototypes.

3.1.3. Kinetics

Experimental measurements were undertaken on the activated $CaCO_3$-Al_2O_3 (20 wt%) storage material decomposition (~1 bar Ar) and CO_2 absorption (~0.8 bar CO_2) using TGA to determine the reactions activation energies. The TGA curves used to determine the peak temperatures are plotted in Fig. S21 (ESI). Kissinger plots derived from different heating rates are presented in Fig. 8. The activation energies for the decomposition and the carbonation are 169 ± 17 and 217 ± 33 kJ.mol^{-1}, respectively. The activation energy of the decomposition agrees with previous kinetics studies of limestone calcination under similar experimental conditions, with values ranging from 166 to 181 kJ.mol^{-1} [49,50]. Thus, the presence of $Ca_xAl_yO_z$ does not directly enhance the decomposition kinetics. The CO_2 absorption activation energy is concordant with the activation energy results between 200 and 230 kJ.mol^{-1} calculated by Grasa et al. for recarbonation; assuming a combined reaction mechanism of the chemical reaction control step and CO_2 diffusion through the carbonate product layer [51]. A numerical study by Mathew et al. fits the carbonation of the $CaCO_3$-Al_2O_3 system with the Avrami nucleation growth model with exponent 3, and identified pressure, temperature, and thermal conductivity of the material being influencing parameters of the reaction kinetics [52]. Mathew et al. calculated the activation energy for carbonation at pressure between 0.6 and 0.8 bar to be ~217 kJ.mol^{-1}, which is verified by the experimental results of this study [52]. The activation energy of the carbonation determined here is similar to pure calcium carbonate. Thus, the presence of $Ca_xAl_yO_z$ does not affect the reaction activation energy during either CO_2 release or absorption.

The results from the present study conclude that the calcium aluminates do not affect the thermodynamics and kinetics of the activated $CaCO_3$-Al_2O_3 (20 wt%) system. Instead, the $Ca_xAl_yO_z$ advantage is solely morphological. The presence of the additive in the storage material matrix allows for carbon dioxide diffusion and maintains the reactive surface area, which hinders the degradation of the sorption capacity over cycles. The thermodynamics, kinetics and cycling capacity confirm the suitability of the system for a scale-up to TCB prototypes.

3.2. Thermochemical battery prototypes

3.2.1. Prototypes sorption capacity

The position of the metallic rod inside the reactor and of the thermocouples along the rod are detailed in Fig. 9. The operating temperature for the cycling of the prototypes were chosen according to the equilibrium diagram determined earlier (Fig. S19, ESI). The temperature of the 'background furnace' was set so that the temperature of the storage material in the reactor was ≈ 900 °C during both charging and discharging steps. That temperature is high enough to trigger the material decomposition at ~0.5 bar, which was the lowest pressure the compressor could achieve; and low enough to allow for the carbonation at ~2 bar CO_2. The temperature of the 'dynamic furnace' was set to 950 °C during charging to compensate for the heat losses through the endothermic decomposition reaction. During discharging, the 'dynamic furnace' was set to 450 °C to allow for the heat to flow out of the reactor through the metallic rods assuming steady state conduction. The step time was set to 6 h to ensure the completion of the decomposition and carbonation reactions and match the demand for energy supply backup in power production plants.

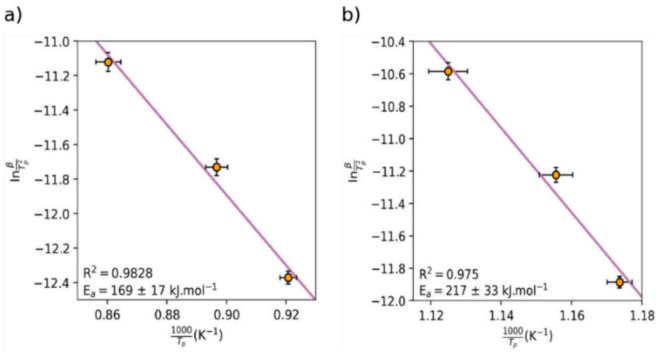

Fig. 8. Kissinger plots determining the activation energy of reaction for a) decomposition (~1 bar Ar), and b) CO_2 absorption (~1 bar CO_2) for the $CaCO_3$-Al_2O_3 (20 wt%) system.

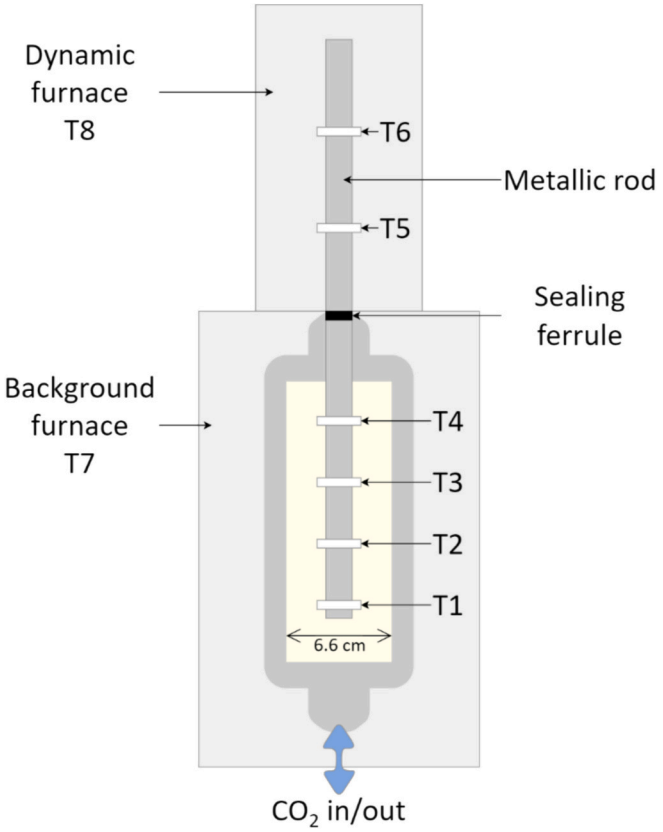

Fig. 9. Unscaled schematic of the prototypes showing the position of the rod inside the reactor and the thermocouples along the metallic rod.

Fig. 10 presents the experimental data collected for prototype 1 (SS rod). The system was fully decomposed prior to the start of the experiment; thus, the cycling study began with an absorption. Fig. 10-a) shows the evolution of the ab/desorption CO_2 capacity over 35 cycles. The carbon dioxide absorption capacity peaks at 37 % of the theoretical maximum on the first cycle, then decreases over time with the system working at a stable maximum capacity of 20 %. Fig. 10-b) presents the variation of the gas pressure in the system/reactor and the resulting pressure variation in the gas storage cylinder.

At the start of the experiment, a CO_2 overpressure of 3 bar (black line in Fig. 10-b, above the desired 2 bar) in the system is attributed to the irreversible formation of the $Ca_xAl_yO_z$. From the 20th cycle, during the absorption step, the pressure in the gas cylinder drops below 2 bar, due to a minor gas leak. The subsequent pressure drop in the system restricts further carbonation. Consequently, after the 30th cycle, the CO_2 pressure in the gas cylinder was refilled to 4 bar, resulting in raising the absorption capacity back to 20 % of the maximum capacity.

Fig. S22-a) (ESI) focusses upon one desorption and absorption cycle and illustrates the reaction kinetics of the material in the reactor, which are in stark contrast to those observed on mg-scale samples used in TGA

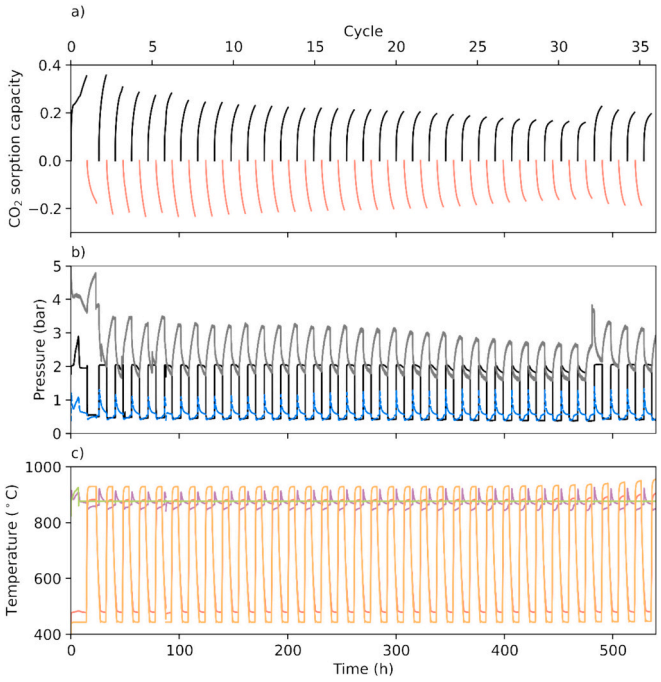

Fig. 10. Prototype 1 (a) cycling capacity, (b) system pressures (black: reactor pressure (P2) and grey: pressure in the gas cylinder (P1), blue: calculated equilibrium pressure at T1) and (c) temperature variation (purple: T1, orange: T5, red: 'dynamic furnace' (T8) and green: 'background furnace' (T7)). (For interpretation of the references to colour in this figure legend, the reader is referred to the web version of this article.)

analysis or those in g-scale Sieverts cycling (Fig. 4). Therefore, the size of the powder-bed in the prototype reactor clearly plays a large role in the achievable reaction kinetics. It is expected that the kinetics are in-fact governed by the ability for the powder-bed to transfer reaction heat to and from the surroundings and/or heat extraction rod. The CO_2 desorption rate was partially limited by the compressor that was used to extract CO_2 from the reactor to the gas storage bottle. However, in most cases the pressure was still able to be maintained at 0.5 bar indicating that the reaction had adequate thermodynamic driving force to proceed but was still not complete in the 6 h step. The absorption first shows a fast reaction step followed by a slower step but was unable to reach completion within the allocated 6 h reaction step. The observed absorption kinetics agrees with the previously reported carbonation mechanism; where in Fig. S22 (ESI), a rapid absorption corresponding to the chemical reaction controlled step of the mechanism occurred within the first hour, while the slower carbon dioxide diffusion through the carbonate layer seems to last during the rest of the discharging [53].

Fig. 10-c) illustrates the temperature at position T7, inside the 'background furnace' measured during the experiment, the programmed temperature variations of the 'dynamic furnace' (T8), the temperature along the heat extraction rod inside the reactor (T1), and in the dynamic furnace (T5). The temperatures measured are consistent over the experiment, displaying no degradation or trends during cycles, which also indicates no deterioration of the thermal conductivity of the metallic rod. A temperature spike of ≈ 50 °C is observed in the reactor (at the rod, T1) during the discharging, when the exothermic absorption reaction is triggered by CO_2 entering the system. The temperature measured along the heat extraction rod at T5 reached 500 °C during the discharging (absorption) of the prototype, which is above the background level of 450 °C in the 'dynamic furnace'. Thus, during discharging the SS heat extraction rod allowed for measurable heat extraction flow from the reactor.

During charging (desorption), the temperature of the 'background furnace' was stabilised at 900 °C, but a temperature of 850 °C was measured in the reactor (at the rod, T1) during the endothermic desorption of CO_2. The thermal signature observed at T1 during CO_2 release has a different relationship over time compared to during CO_2 absorption. CO_2 absorption resulted in a thermal spike followed by exponential decay, whereas CO_2 release showed a more uniform temperature over time, illustrating a difference in the reaction kinetics in the reactor. The thermodynamic equilibrium pressure of the $CaCO_3$-CaO/CO_2 system at 850 °C is ≈ 0.5 bar, implying that the reactor became reaction limited under these operating conditions and could not continue to release CO_2 until heat was able to be supplied by the heat extraction rod (or surroundings). That is, the observed reaction kinetics in the reactor were governed by heat transfer, rather than inherent chemical reaction kinetics.

Fig. 11 presents the data from the cycling experiment for prototype 2 (SS tube with the copper core). Conversely to the cycling of prototype 1, the initial desorption step was recorded. During the first 10 cycles, the operating conditions were adjusted according to the observations from the previous prototype to obtain optimal cycling conditions and observed activation of the material. To increase the driving force of CO_2 desorption during the charging process, the temperature of the background furnace was raised to 950 °C to effectively reach 900 °C (1.2 bar reaction equilibrium pressure) inside the reactor (T1). Initially, the pressure inside the gas cylinder was above 4 bar, which was too high for the gas booster to reduce the system pressure to below 0.5 bar during the desorption step. Overall, a starting pressure in the cylinder between 3 and 4 bar before the onset of absorption allows for maintaining a system pressure of >2 bar during the entire discharging (absorption) process, and for the compressor to achieve pressures <0.5 bar during charging (desorption).

Fig. 11-a) shows that the absorption capacity peaked at 28 % of the maximum capacity on the 13th cycle. The following cycles exhibit a decreasing trend in capacity, similar to prototype 1, reaching 20 % capacity as well. The blue line on Fig. 11-b) indicates the equilibrium pressure. Desorption was complete once the pressure was lower than the

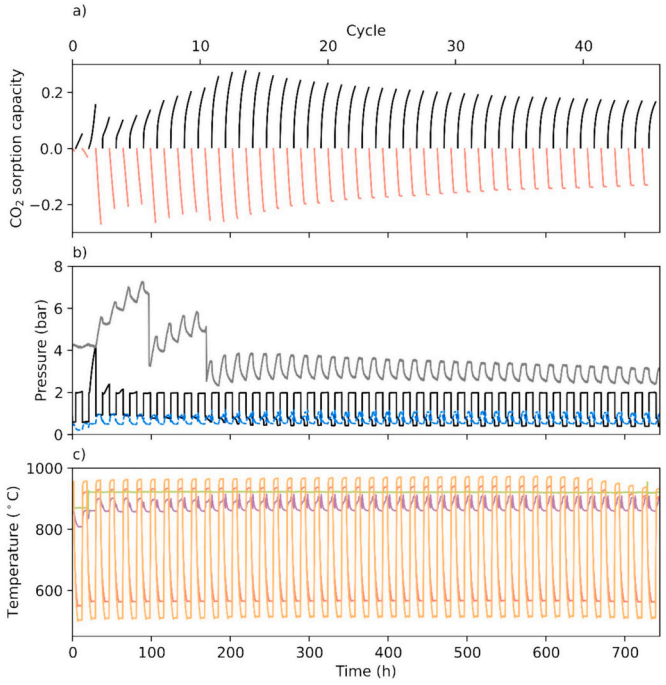

Fig. 11. Prototype 2 (a) cycling capacity, (b) system pressures (black: reactor pressure (P2) and grey: pressure in the gas cylinder (P1), blue: calculated equilibrium pressure at T1) and (c) temperature variation (purple: T1, orange: T5, red: 'dynamic furnace' and green: 'background furnace'). (For interpretation of the references to colour in this figure legend, the reader is referred to the web version of this article.)

equilibrium pressure during this step. The kinetics data for the 13th cycle illustrated in Fig. S22-b) (ESI) confirms the completion of the desorption step, showing a flattened curve after 4 h. Therefore, the loss in capacity seems to result from the incomplete carbonation of the material within the 6 h discharging step. The system absorbed slightly more CO_2 than it desorbed during each cycle, which can be caused by impurities in the as-supplied CO_2 gas. Since gas volumes are measured using a mass flow meter, impurities in the gas cylinder would be measured upon absorption. However, the gas desorbed upon the desorption step should only be carbon dioxide because the impurities are not likely to remain in the system after exposure to high temperatures; thus, the amount of gas measured during the desorption step truly reflects the capacity of the system. Fig. 11-c) shows the temperatures measured at T1 and T5, as well as the 'background' and 'dynamic furnace' temperatures. During the discharging, the heat extraction rod (SS tube with the copper core) allowed for T5 to reach 580 °C, which is 130 °C higher than the set temperature of the dynamic furnace during that step. T1 varies between 900 and 870 °C during charging and discharging, respectively. The higher temperature observed at T5 compared to prototype 1 displays the higher heat flow rate of the copper compared to SS, and thus allowed for more rapid CO_2 desorption.

Previous cycling of pure $CaCO_3$ has shown capacity to be reduced drastically over the first 15 cycles, of which is attributed to sintering and pore plugging issues [13,19–22]. In the present study, the low absorption capacity in both prototypes compared to the theoretical maximum may instead be linked to a temperature gradient within the reactor bed. The low thermal conductivity of the storage material (2.3 and 0.8 W.m^{-1}.K^{-1} for $CaCO_3$ and CaO, respectively [54]) may contribute to a strong radial temperature gradient within the reactor. According to a modelling study by Mathew et al., the thermal conductivity of the storage material influences the reaction conversion rate [52]. Assuming that the temperature could reach 935 °C in some part of the reactor bed during the discharging (matching an equilibrium pressure of 2 bar equal to the system pressure), a higher pressure of carbon dioxide is required to guarantee the absorption reaction to occur.

Following the cycling, prototype 2 was subjected to an additional experiment to verify the aforementioned hypothesis that temperature gradients exist within the reactor bed. The absorption capacity was measured at a CO_2 pressure of 3 and 4 bar, while collecting the temperature data on the external wall of the reactor (inside insulation layer) to assess the radial temperature distribution within the reactor bed. A pressure of 4 bar during absorption led to double the carbon dioxide absorption capacity, whereas similar capacities were achieved at 2 and 3 bar (Fig. 12). However, after the first absorption at 4 bar, the system failed to undergo further absorption. The temperature measured on the external wall of the reactor was steady at ≈ 1000 °C. Thus, there is a 100 °C difference between the temperatures measured by the thermocouples placed along the rod in the centre of the material and the reactor wall, which confirms the assumption of the existence of a strong radial temperature gradient within the storage material.

The temperature gradient within the reactor bed is likely to affect the absorption capacity. According to the equilibrium diagram (Fig. S19, ESI) at 1000 °C and 4 bar, the carbonation of the material should occur because those conditions are above the equilibrium curve. Thus, it is not yet clear what hindered further cycling of the system discharging at 4 bar.

The following section presents XRD characterisation of the storage material from both prototypes after the cycling experiments, aiming to provide explanations for the aforementioned observations. Samples were collected from five zones of the reactor bed from the bottom to the top and on the side (closer to the reactor wall) of both prototypes. Fig. S23-a) illustrates the sample collection and Fig. S23-b) and c) shows the corresponding XRD patterns for prototypes 1 and 2, respectively.

Fig. 13 illustrates the quantitative Rietveld refinement results for each sample for (a) prototype 1 after ~550 h cycling and (b) prototype 2 after ~750 h cycling and absorption test at 4 bar. The refined phase

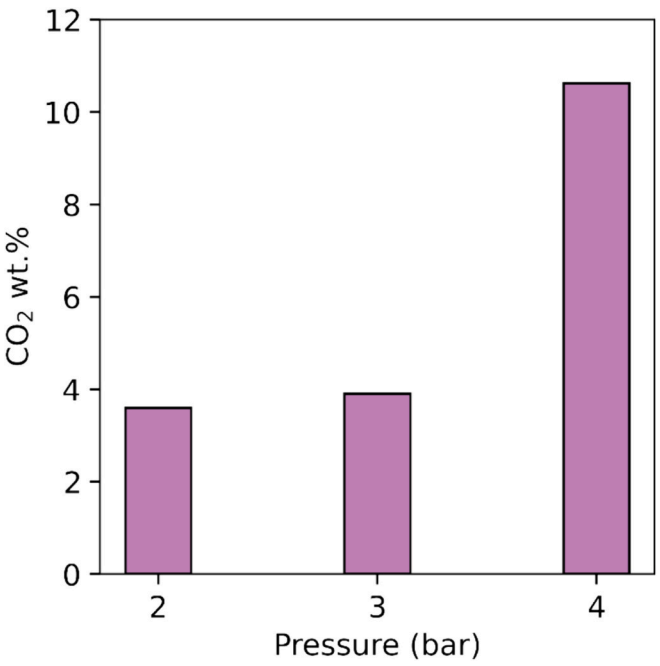

Fig. 12. Comparison of the CO_2 absorption capacity of Prototype 2 at different pressure.

compositions are summarised in Table S2 (ESI). Both experiments ended after a CO_2 absorption step, therefore each sample was expected to be carbonated. The samples from prototype 1 (Fig. 13-a) contain various proportions of calcium carbonate and calcium oxide depending on the location of the sample in the reactor bed, which indicates only partial carbonation of the whole system. In prototype 1, $Ca_5Al_6O_{14}$ and $Ca_{12}Al_{14}O_{33}$ constitute ~20 wt% and up to ~30 wt% of the storage material composition, respectively. The variation in the sample compositions correlates with the temperature gradient within the reactor bed, vertically and radially. The high Mayenite content led to lower carbonation rate, which, according to a DFT study reported by Ma et al., is explained by the strong binding interaction between CaO and $Ca_{12}Al_{14}O_{33}$ that may contribute to the deactivation of the oxide sorption capacity in addition to the increased consumption of CaO to form the Mayenite [26]. Both prototypes achieved similar cyclic capacity during the cycling experiments; thus, it is assumed that prototype 2 would exhibit an analogous composition after 750 h cycling. The powder samples extracted from prototype 2 after the cycling and the absorption tests at 4 bar and 900 °C (Fig. 13-b) have homogeneous compositions and do not contain any significant amount of $CaCO_3$ or $Ca_5Al_6O_{14}$. Instead, the samples contain ~40 wt% of CaO and ~50 wt% of $Ca_{12}Al_{14}O_{33}$ (Mayenite). The small amount (~3 wt%) of $Ca_9Al_6O_{18}$ probably results from a subsequent reaction of Al_2O_3 with CaO (eq. 11) [26].

Mayenite is known to form when the temperature exceeds 1000 °C [27,55]. Therefore, the most likely cause of the large Mayenite formation during the absorption at 4 bar of carbon dioxide is overheating of the storage material during the exothermic process. Thus, high temperatures within the powder-bed should be avoided to restrict Mayenite formation and maintain a higher cyclic capacity and better reaction kinetics.

Over 30 cycles, both prototypes share a similar trend for the degradation of the cycling capacity. Interestingly, the decline in sorption capacity is worse than that observed in the initial storage material study above (Fig. 4). The low operating capacity (20 % for the prototypes versus 60 % in the initial storage material study) suggests that the storage material only partially cycled in the prototypes due to the operating conditions, especially thermal gradients throughout the

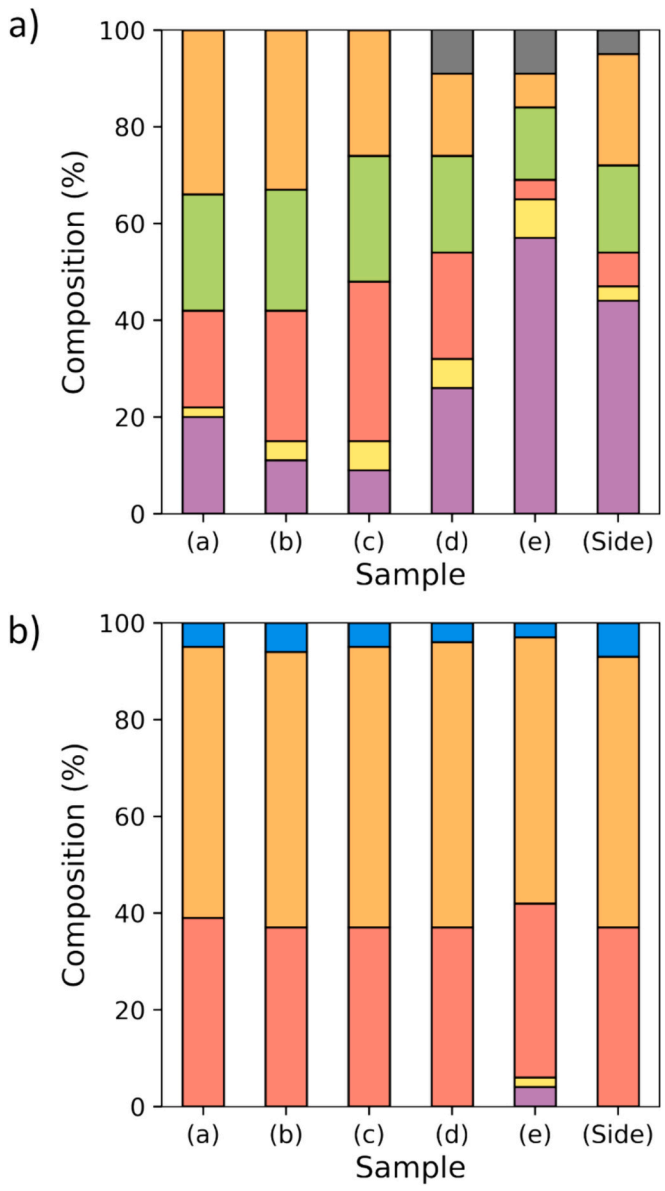

Fig. 13. Composition of the samples collected from: (a) Prototype 1 after ~550 h cycling; (b) Prototype 2 following the ~750 h cycling and absorption experiment at a CO_2 pressure of 4 bar, with samples (a) to (e) from the reactor bottom to the top and on the side close to the bottom reactor wall. $CaCO_3$: purple; Al_2O_3: yellow; CaO: red; $Ca_5Al_6O_{14}$: green; $Ca_{12}Al_{14}O_{33}$: orange; $CaAl_2O_4$: grey; $Ca_9Al_6O_{18}$: blue. (For interpretation of the references to colour in this figure legend, the reader is referred to the web version of this article.)

powder bed. Charging can be improved by operating at a higher temperature to increase the equilibrium pressure of the $CaCO_3$, but this could lead to adverse grain growth, sintering, and possible Mayenite formation. Nevertheless, higher temperatures hinder the CO_2 absorption capacity during discharging and requires higher operating pressure, which in turn, promotes Mayenite formation due to temperature runaway. Lowering the operating temperature promotes the optimal absorption capacity and preserves the storage material, but a gas booster with a higher compression ratio would be required to enable decomposition close to vacuum conditions. In particular, the poor thermal conductivity of the storage material is an issue to solve as to maintain a homogeneous temperature within the reactor bed, which may avoid overheating of the powder bed and/or thermal gradients. These observations highlight the key role of the heat extraction unit to manage the temperature within the reactor during the charging and discharging of the TCB prototypes.

3.2.2. *Quantitative assessment of the heat extraction*

Fig. 14 displays a heat map of the average temperature measured over cycles during: (a) the desorption (charging), and (b) the absorption (discharging). During charging (Fig. 13-a), both prototypes exhibit relatively uniform temperatures inside the reactor (T1 – T4). The 'background furnace' temperatures remain the same during both steps. During discharging (Fig. 14-b), there are temperature gradients of ~50 °C within the reactor along the heat extraction rods. This temperature has an impact on the performance of the TCES material due to its temperature dependent equilibrium pressure. However, the large temperature difference (~250 °C) between the inside of the reactor (T1–T4) and the inside of the dynamic furnace (T5–T6) indicates the slow heat transfer rates of both metallic rods. Noticeably, the SS tube with the copper core in prototype 2 allows for a smoother distribution of the temperatures along its length, demonstrating better heat extraction performance than the SS rod in prototype 1. During discharging, the 'dynamic furnace' is set to 450 °C. The SS rod in prototype 1 allows for a temperature rise in the dynamic furnace of only 6 °C, whereas the SS tube with the copper core in prototype 2 raised the dynamic furnace temperature by 78 °C.

According to eq. 5 and considering the effective capacity of the prototypes to be 20 %, the energy storage capacity of prototype 1 and 2, respectively are 1132 and 1007 kJ, corresponding to a power of 52 and 47 W_{th} over 6 h. The heat flux and the heat transfer rate determined using eqs. 6–8 for each prototype are summarised in Table 3. The heat transfer rates are limited by the properties of the metallic rods. During charging, the heat transfer rates of 0.7 and 8 W for prototype 1 and 2, respectively, are insufficient to cover the heat losses triggered by the endothermic reaction, signifying that the temperature of the storage material drops. However, during the discharging, the heat transfer rate of prototype 2 (50 W) is above the amount of heat generated by the storage material; thus, the SS tube with copper rod enabled the heat extraction. Conversely, it is not the case for prototype 1, for which the discharge heat rate reached only 3 W.

The evaluation of the heat transfer rate by conduction indicates that the SS rod in prototype 1 failed to extract heat efficiently. Yet, the SS tube with a copper core in prototype 2 allowed for a sufficient heat transfer rate to raise the temperature in the dynamic furnace up to ~530 °C. This is in the optimal temperature range of a 1 kWh Stirling engine. However, this Stirling engine requires 4 kWh_{th} to reach 1 $kWh_{electric}$ output (25 % efficiency), which means that the power required to run the engine for 6 h is 667 W_{th}. The discharging heat transfer rate of prototype 2 was limited to 50 W by the rod (7 % of the targeted power). This scale of TCB prototype would allow for the engine to run for only 25 min. It is likely that a larger system with heat extraction by conduction through a SS tube with a copper core could ensure power production by a Stirling engine. However, the low cycling capacity demonstrated by those prototypes must be addressed to guarantee the performance of the battery over time. Different reactor designs could promote heat circulation through the storage material, thereby enhancing the sorption capacity [56].

In this paper, the design of the reactor implies that the distance between the metallic rod and the storage material is >2 cm. The heat transfer could be enhanced by reducing the distance between the material and the heat extraction unit and by increasing the heat exchange surface area, for example by using thin plate heat exchangers. Additives with high thermal conductivity could also be considered, but it would reduce the overall capacity. The design of TCB prototypes depend on the constraints set by the storage material. For example, high-temperature materials are limiting the options of heat extraction systems, as is the case with the metal carbonates in the present work. Different prototype designs with more efficient heat extraction system, such as convection, are conceivable for other types of TCES systems operating at lower temperatures, including certain metal hydrides, hydroxides, and redox

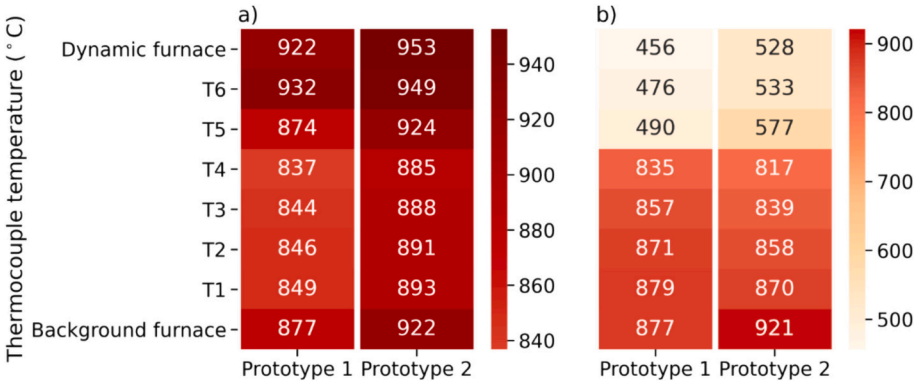

Fig. 14. Heatmaps comparing the temperature gradients of prototypes 1 and 2 during (a) desorption (charging) and (b) absorption (discharging). T1–T4 are temperatures measured inside the reactor, while T5 and T6 are temperatures collected from the thermocouples placed along the external metallic rod residing inside the 'dynamic furnace'.

Table 3
Determination of the heat flux and heat transfer rate for each prototype.

	Prototype 1	Prototype 2
Energy storage capacity [kJ]	1132	1007
Power capacity over 6 h [W_{th}]	52	47
Rod cross-section area [x 10^{-4}.m^2]	2.01	2.84
T1 – T6 distance [m]	0.63	0.63
κ [$W.m^{-1}.K^{-1}$]	26	329
Charging heat flux q_c [kW. m^{-2}]	3	28
Charging heat transfer rate Q_c [W]	0.7	8
Discharging heat flux q_d [kW. m^{-2}]	17	176
Discharging heat transfer rate Q_d [W]	3	50

materials.

3.2.3. *Prototype corrosion*

Prototypes 1 and 2 cycled near 900 °C for ~550 h and ~750 h, respectively. In both cases, corrosion was observed on the outer SS reactor body and the external surface of the heat extraction rod. The outer surface of the reactor and the part of the rod exposed to air both exhibited flake exfoliation, while the inner surface of the reactor and the part of the rod exposed to CO_2 showed dealloying and intergranular attack (Fig. S24-a and b, ESI). Similar observations have been described in detail by Møller et al. in a study using a 316L SS reactor [27]. At the end of both experiments, the material in the reactor is predominantly composed of fine white powder similar to the starting material, with some small, agglomerated chunks. The cross-section of the SS heat extraction rod (Fig. S24-c, ESI) shows that the inner volume of the rod has been protected from corrosion by the ~1 mm thick oxide layer on the external surface. XRD analysis of a cross-section of the SS tube with copper core in prototype 2 presented in Fig. S25 (ESI) shows only diffraction peaks corresponding to copper. Thus, the copper core did not degrade during the experiment due to the isolation from the gas through containment in the sealed SS sleeve. Therefore, the thermal conductivity of the rods assumed for the calculations have remained consistent over time.

The use of SS was suitable for the time frame (≤800 h) and operating conditions (≤950 °C and carbon dioxide pressure ≤4 bar) of the experiments. However, for safety and viability of larger systems aiming to operate for longer time periods, the use of more corrosion resistant material, such as Inconel, is recommended [57]. Larger scale systems may use refractory lined reactors, with a lower temperature outer metallic shell that provides gas containment. This would avoid higher cost corrosion resistant metallic containment materials.

4. Conclusion

This study examined the thermodynamics, kinetics, and TCES properties of $CaCO_3$-Al_2O_3 (20 wt%). The thermodynamics of the thermochemical reactions ($\Delta H_{des} = 173 \pm 10$ kJ.mol^{-1} CO_2 and $\Delta S_{des} = 147 \pm 9$ J.mol^{-1} CO_2·K^{-1}) were found to be similar to those of as-supplied calcium carbonate ($\Delta H_{des} = 172 \pm 8$ kJ.mol^{-1} CO_2 and $\Delta S_{des} = 146 \pm 7$ J.mol^{-1} CO_2·K^{-1}). The activation energies of 169 and 217 kJ.mol^{-1} for decomposition and absorption reactions, respectively, were consistent with previous theoretical models defining the reaction kinetics of pure calcium carbonate. The addition of alumina does not affect the thermodynamics and kinetics of the system. The measured sorption capacity of the material exhibited results in line with previous studies on this TCES system (60 % of the theoretical maximum). The physical properties of the $CaCO_3$-Al_2O_3 (20 wt%) were found suitable for a system scale-up.

Two TCB prototypes using a SS rod and a SS tube with a copper core to extract the heat generated during the battery discharging were constructed. Experimental results concerning storage capacity and heat extraction efficiency showed a strong correlation between the system pressure, the temperature, and the carbonation conversion. The sorption capacity of both prototypes was 20 %, revealing only a partial reactivity of the system. A temperature gradient within the reactor bed may contribute to the loss of sorption capacity. The SS rod in prototype 1 failed to effectively transfer heat in and out of the system, whereas the SS tube with a copper core in prototype 2 demonstrated a sufficient heat transfer rate (50 W).

Varying the design of the reactor could address the heat transfer issues within the reactor and maximise the cycling capacity of the battery, by improving the temperature management within the storage material and enhancing its thermal conductivity. For example, multiple rods could go through the reactor, enabling a higher conversion rate and extending the potential use of the Stirling engine. Heat transfer optimisation using numerical modelling should help explore different design options and assess the resulting heat transfer.

Author contributions

The manuscript was written through contributions of all authors. All authors have approved the final version of the manuscript.

CRediT authorship contribution statement

Lucie Desage: Writing – review & editing, Writing – original draft, Methodology, Investigation, Formal analysis, Data curation, Conceptualization. **Terry D. Humphries:** Writing – review & editing, Supervision, Project administration, Methodology, Investigation, Funding

acquisition, Formal analysis, Data curation, Conceptualization. **Mark Paskevicius:** Writing – review & editing, Supervision, Project administration, Methodology, Investigation, Funding acquisition, Formal analysis, Data curation, Conceptualization. **Craig E. Buckley:** Writing – review & editing, Supervision, Project administration, Funding acquisition, Conceptualization.

Declaration of competing interest

Terry Humphries reports financial support was provided by Australian Government Department of Industry Science Energy and Resources. Terry Humphries reports financial support was provided by Australian Research Council. Lucie Desage reports financial support was provided by Australian Government Department of Industry Science Energy and Resources. Mark Paskevicius reports financial support was provided by Australian Research Council. Craig Buckley reports financial support was provided by Australian Research Council. Mark Paskevicius reports financial support was provided by Australian Government Department of Industry Science Energy and Resources. Craig Buckley reports financial support was provided by Australian Government Department of Industry Science Energy and Resources. Lucie Desage reports financial support was provided by Future Energy Exports Cooperative Research Centre.

Data availability

Data will be made available on request.

Acknowledgments

CEB, MP, TDH and LD acknowledge the Department of Industry, Science, Energy and Resources for funding from a 2019 Global Innovation Linkage (GIL73589) grant Round 2. CEB, MP and TDH acknowledge the financial support of the Australian Research Council for ARC Discovery grant DP200102301 and DP230100429. LD acknowledges the support of the Future Energy Exports CRC (www.fenex.org.au) whose activities are funded by the Australian Government's Cooperative Research Centre Program. This is FEnEx CRC Document 2023/22.RP2.0121-PHD-FNX-010. The authors thank Mark Winstanley for his engineering assistance with the prototypes.

Appendix A. Supplementary data

Supplementary data to this article can be found online at https://doi.org/10.1016/j.est.2024.111917.

References

[1] L. Clarke, Y.-M. Wei, A. de la Vega Navarro, A. Garg, A.N. Hahmann, S. Khennas, et al., Energy Systems, in: Climate Change 2022: Mitigation of Climate Change Working Group III Contribution to the IPCC Sixth Assessment Report, Cambridge University Press, 2022.
[2] P.W. Gruber, P.A. Medina, G.A. Keoleian, S.E. Kesler, M.P. Everson, T. J. Wallington, Global Lithium availability, J. Ind. Ecol. 15 (2011) 760–775, https://doi.org/10.1111/j.1530-9290.2011.00359.x.
[3] Nick Florin, E. Dominish, Sustainability Evaluation of Energy Storage Technologies, in: Institute of Sustainable Futures for the Australian Council of Learned Academies, 2017.
[4] K.M. Kennedy, T.H. Ruggles, K. Rinaldi, J.A. Dowling, L. Duan, K. Caldeira, N. S. Lewis, The role of concentrated solar power with thermal energy storage in least-cost highly reliable electricity systems fully powered by variable renewable energy, Advances in Applied Energy. 6 (2022) 100091, https://doi.org/10.1016/j.adapen.2022.100091.
[5] L. Desage, E. McCabe, A.P. Vieira, T.D. Humphries, M. Paskevicius, C.E. Buckley, Thermochemical batteries using metal carbonates: A review of heat storage and extraction, Journal of Energy Storage. 71 (2023) 107901, https://doi.org/10.1016/j.est.2023.107901.
[6] M. Papapetrou, G. Kosmadakis, A. Cipollina, U. La Commare, G. Micale, Industrial waste heat: estimation of the technically available resource in the EU per industrial sector, temperature level and country, Appl. Therm. Eng. 138 (2018) 207–216, https://doi.org/10.1016/j.applthermaleng.2018.04.043.
[7] L. Poupin, T.D. Humphries, M. Paskevicius, C.E. Buckley, A thermal energy storage prototype using sodium magnesium hydride, Sustainable Energy Fuels 3 (2019) 985–995, https://doi.org/10.1039/c8se00596f.
[8] L. Poupin, T.D. Humphries, M. Paskevicius, C.E. Buckley, An experimental high temperature thermal battery coupled to a low temperature metal hydride for solar thermal energy storage, Sustain Energy Fuels. 4 (2020) 285–292, https://doi.org/10.1039/c9se00538b.
[9] L. Poupin, T.D. Humphries, M. Paskevicius, C.E. Buckley, An operational high temperature thermal energy storage system using magnesium iron hydride, Int. J. Hydrog. Energy 46 (2021) 38755–38767, https://doi.org/10.1016/j.ijhydene.2021.09.146.
[10] G. Lundholm, The Experimental V4X Stirling Engine – A Pioneering Development, 2003.
[11] A.J. Carrillo, J. González-Aguilar, M. Romero, J.M. Coronado, Solar energy on demand: A review on high temperature thermochemical heat storage systems and materials, Chem. Rev. 119 (2019) 4777–4816, https://doi.org/10.1021/acs.chemrev.8b00315.
[12] A.H. Abedin, M.A. Rosen, A critical review of thermochemical energy storage systems, The Open Renewable Energy Journal 4 (2011), https://doi.org/10.2174/1876387101004010042.
[13] J. Sunku Prasad, P. Muthukumar, F. Desai, D.N. Basu, M.M. Rahman, A critical review of high-temperature reversible thermochemical energy storage systems, Appl. Energy 254 (2019) 113733, https://doi.org/10.1016/j.apenergy.2019.113733.
[14] A. Bayon, R. Bader, M. Jafarian, L. Fedunik-Hofman, Y. Sun, J. Hinkley, et al., Techno-economic assessment of solid–gas thermochemical energy storage systems for solar thermal power applications, Energy 149 (2018) 473–484, https://doi.org/10.1016/j.energy.2017.11.084.
[15] K.T. Møller, A. Ibrahim, C.E. Buckley, M. Paskevicius, Inexpensive thermochemical energy storage utilising additive enhanced limestone, J. Mater. Chem. A 8 (2020) 9646–9653, https://doi.org/10.1039/D0TA03080E.
[16] A. Reller, R. Emmenegger, C. Padeste, H.-R. Oswald, Thermochemical reactivity of metal carbonates, CHIMIA Int. J. Chem. 45 (1991) 262–266, https://doi.org/10.2533/chimia.1991.262.
[17] M. Benitez-Guerrero, J.M. Valverde, P.E. Sanchez-Jimenez, A. Perejon, L.A. Perez-Maqueda, Multicycle activity of natural $CaCO_3$ minerals for thermochemical energy storage in concentrated solar power plants, Sol. Energy 153 (2017) 188–199, https://doi.org/10.1016/j.solener.2017.05.068.
[18] B. Sarrión, A. Perejón, P.E. Sánchez-Jiménez, N. Amghar, R. Chacartegui, J. Manuel Valverde, L.A. Pérez-Maqueda, Calcination under low CO_2 pressure enhances the calcium looping performance of limestone for thermochemical energy storage, Chem. Eng. J. (2020) 127922, https://doi.org/10.1016/j.cej.2020.127922.
[19] M. Benitez-Guerrero, B. Sarrion, A. Perejon, P.E. Sanchez-Jimenez, L.A. Perez-Maqueda, J. Manuel Valverde, Large-scale high-temperature solar energy storage using natural minerals, Sol. Energy Mater. Sol. Cells 168 (2017) 14–21, https://doi.org/10.1016/j.solmat.2017.04.013.
[20] F.J. Durán-Olivencia, M.J. Espín, J.M. Valverde, Cross effect between temperature and consolidation on the flow behavior of granular materials in thermal energy storage systems, Powder Technol. 363 (2020) 135–145, https://doi.org/10.1016/j.powtec.2019.11.125.
[21] W. Liu, H. An, C. Qin, J. Yin, G. Wang, B. Feng, M. Xu, Performance enhancement of calcium oxide sorbents for cyclic CO_2 capture – A review, Energy Fuel 26 (2012) 2751–2767, https://doi.org/10.1021/ef300220x.
[22] B.R. Stanmore, P. Gilot, Review – calcination and carbonation of limestone during thermal cycling for CO_2 sequestration, Fuel Process. Technol. 86 (2005) 1707–1743, https://doi.org/10.1016/j.fuproc.2005.01.023.
[23] R. Chacartegui, A. Alovisio, C. Ortiz, J.M. Valverde, V. Verda, J.A. Becerra, Thermochemical energy storage of concentrated solar power by integration of the calcium looping process and a CO_2 power cycle, Appl. Energy 173 (2016) 589–605, https://doi.org/10.1016/j.apenergy.2016.04.053.
[24] M. Aihara, T. Nagai, J. Matsushita, Y. Negishi, H. Ohya, Development of porous solid reactant for thermal-energy storage and temperature upgrade using carbonation/decarbonation reaction, Appl. Energy 69 (2001) 225–238, https://doi.org/10.1016/s0306-2619(00)00072-6.
[25] J.M. Valverde, A. Perejon, L.A. Perez-Maqueda, Enhancement of fast CO_2 capture by a Nano-SiO_2/CaO composite at ca-looping conditions, Environ. Sci. Technol. 46 (2012) 6401–6408, https://doi.org/10.1021/es3002426.
[26] X. Ma, X. Huang, H. Zhang, X. Hu, T. Feng, Effect of calcium aluminates on the structure evolution of CaO during the calcium looping process: A DFT study, Chem. Eng. J. 452 (2023) 139552, https://doi.org/10.1016/j.cej.2022.139552.
[27] K.T. Møller, T.D. Humphries, A. Berger, M. Paskevicius, C.E. Buckley, Thermochemical energy storage system development utilising limestone, Chemical Engineering Journal Advances. 8 (2021) 100168, https://doi.org/10.1016/j.ceja.2021.100168.
[28] I. Arias, J. Cardemil, E. Zarza, L. Valenzuela, R. Escobar, Latest developments, assessments and research trends for next generation of concentrated solar power plants using liquid heat transfer fluids, Renew. Sust. Energ. Rev. 168 (2022) 112844, https://doi.org/10.1016/j.rser.2022.112844.
[29] K. Vignarooban, X. Xu, A. Arvay, K. Hsu, A.M. Kannan, Heat transfer fluids for concentrating solar power systems – A review, Appl. Energy 146 (2015) 383–396, https://doi.org/10.1016/j.apenergy.2015.01.125.
[30] A. Heinzel, W. Hering, J. Konys, L. Marocco, K. Litfin, G. Müller, et al., Liquid metals as efficient high-temperature heat-transport fluids, Energ. Technol. 5 (2017) 1026–1036, https://doi.org/10.1002/ente.201600721.

[31] N. Lorenzin, A. Abánades, A review on the application of liquid metals as heat transfer fluid in concentrated solar power technologies, Int. J. Hydrog. Energy 41 (2016) 6990–6995, https://doi.org/10.1016/j.ijhydene.2016.01.030.
[32] M.T. White, G. Bianchi, L. Chai, S.A. Tassou, A.I. Sayma, Review of supercritical CO_2 technologies and systems for power generation, Appl. Therm. Eng. 185 (2021) 116447, https://doi.org/10.1016/j.applthermaleng.2020.116447.
[33] M. Pelanconi, M. Barbato, S. Zavattoni, G.L. Vignoles, A. Ortona, Thermal design, optimization and additive manufacturing of ceramic regular structures to maximize the radiative heat transfer, Mater. Des. 163 (2019) 107539, https://doi.org/10.1016/j.matdes.2018.107539.
[34] D.A. Sheppard, M. Paskevicius, P. Javadian, I.J. Davies, C.E. Buckley, Methods for accurate high-temperature Sieverts-type hydrogen measurements of metal hydrides, J. Alloys Compd. 787 (2019) 1225–1237, https://doi.org/10.1016/j.jallcom.2019.02.067.
[35] E. Lemmon, I.H. Bell, M. Huber, M. McLinden, NIST Standard Reference Database 23: Reference Fluid Thermodynamic and Transport Properties-REFPROP, Version 10.0, National Institute of Standards and Technology. Standard Reference Data Program, Gaithersburg, 2018.
[36] T. Renner, Quantities, Units and Symbols in Physical Chemistry, The Royal Society of Chemistry, 2007.
[37] H.E. Kissinger, Reaction kinetics in differential thermal analysis, Anal. Chem. 29 (1957) 1702–1706, https://doi.org/10.1021/ac60131a045.
[38] H.M. Rietveld, A profile refinement method for nuclear and magnetic structures, J. Appl. Crystallogr. 2 (1969) 65–71, https://doi.org/10.1107/s0021889869006558.
[39] A.A. Coelho, *TOPAS* and *TOPAS-academic*: an optimization program integrating computer algebra and crystallographic objects written in C++, J. Appl. Crystallogr. 51 (2018) 210–218, https://doi.org/10.1107/s1600576718000183.
[40] B. Schmitt, C. Bronnimann, E.F. Eikenberry, F. Gozzo, C. Hormann, R. Horisberger, B. Patterson, Mythen detector system, Nucl Instrum Meth A. 501 (2003) 267–272, https://doi.org/10.1016/S0168-9002(02)02045-4.
[41] S. Rudtsch, H.P. Ebert, F. Hemberger, G. Barth, R. Brandt, U. Groß, et al., Intercomparison of Thermophysical property measurements on an austenitic stainless steel, Int. J. Thermophys. 26 (2005) 855–867, https://doi.org/10.1007/s10765-005-5582-6.
[42] The Engineering Toolbox, Metals, Metallic Elements and Alloys - Thermal Conductivities. https://www.engineeringtoolbox.com/thermal-conductivity-metals-d_858.html; accessed 08/04/2024.
[43] G.A. Greene, Heat transfer, in: R.A. Meyers (Ed.), Encyclopedia of Physical Science and Technology (Third Edition), Academic Press, New York, 2003, pp. 279–292.
[44] N.J. Tannyan, G. Plascencia, T.A. Utigard, High temperature oxidation of copper and copper aluminum alloys, Can. Metall. Q. 41 (2002) 213–218, https://doi.org/10.1179/cmq.2002.41.2.213.
[45] Y. Wan, X. Wang, H. Sun, Y. Li, K. Zhang, Y. Wu, Corrosion Behavior of Copper at Elevated Temperature, 2012.
[46] S. Lux, G. Baldauf-Sommerbauer, M. Siebenhofer, Hydrogenation of inorganic metal carbonates: A review on its potential for carbon dioxide utilization and emission reduction, ChemSusChem 11 (2018) 3357–3375, https://doi.org/10.1002/cssc.201801356.
[47] Z. Zhu, T. Jiang, G. Li, Y. Guo, Y. Yang, Thermodynamics of Reactions Among Al_2O_3, CaO, SiO_2 and Fe_2O_3 During Roasting Processes, in: Juan Carlos Moreno-Pirajan (Ed.), Thermodynamics - Interaction Studies - Solids, Liquids and Gases, InTech, 2011, pp. 825–838.
[48] HSC Chemistry v. 9, https://www.metso.com/portfolio/hsc-chemistry/; 2021 [accessed 08/04/2024].
[49] I. Ar, G. Doğu, Calcination kinetics of high purity limestones, Chem. Eng. J. 83 (2001) 131–137, https://doi.org/10.1016/S1385-8947(00)00258-8.
[50] F. García-Labiano, A. Abad, L.F. de Diego, P. Gayán, J. Adánez, Calcination of calcium-based sorbents at pressure in a broad range of CO_2 concentrations, Chem. Eng. Sci. 57 (2002) 2381–2393, https://doi.org/10.1016/S0009-2509(02)00137-9.
[51] G. Grasa, I. Martínez, M.E. Diego, J.C. Abanades, Determination of CaO carbonation kinetics under recarbonation conditions, Energy & Fuels 28 (2014) 4033–4042, https://doi.org/10.1021/ef500331t.
[52] A. Mathew, N. Nadim, T.T. Chandratilleke, M. Paskevicius, T.D. Humphries, C. E. Buckley, Kinetic investigation and numerical modelling of $CaCO_3$/$Al2O_3$ reactor for high-temperature thermal energy storage application, Sol. Energy 241 (2022) 262–274, https://doi.org/10.1016/j.solener.2022.06.005.
[53] C. Ortiz, J.M. Valverde, R. Chacartegui, L.A. Perez-Maqueda, Carbonation of limestone derived CaO for thermochemical energy storage: from kinetics to process integration in concentrating solar plants, ACS Sustain. Chem. Eng. 6 (2018) 6404–6417, https://doi.org/10.1021/acssuschemeng.8b00199.
[54] J.E. Bird, T.D. Humphries, M. Paskevicius, L. Poupin, C.E. Buckley, Thermal properties of thermochemical heat storage materials, Phys. Chem. Chem. Phys. 22 (2020) 4617–4625, https://doi.org/10.1039/c9cp05940g.
[55] A. Intiso, F. Rossi, A. Proto, R. Cucciniello, The fascinating world of mayenite ($Ca_{12}Al_{14}O_{33}$) and its derivatives, Rendiconti Lincei Scienze Fisiche e Naturali. 32 (2021) 699–708, https://doi.org/10.1007/s12210-021-01025-w.
[56] M. Wild, L. Lüönd, A. Steinfeld, Experimental investigation of a thermochemical reactor for high-temperature heat storage via carbonation-calcination based cycles, Frontiers in Energy Research 9 (2021) 748665, https://doi.org/10.3389/fenrg.2021.748665.
[57] L. Shoemaker, Alloys 625 and 725: Trends in Properties and Applications, in: E. A. Loria (Ed.), Superalloys 718, 625, 706 and Derivatives Proceedings of the Sixth International Symposium on Superalloys 718, 625, 706 and Derivatives, 2005, pp. 409–418.